scientific reports

Check for updates

OPEN

Highly accurate calculation of electric field for transcranial magnetic stimulation using hybridizable discontinuous galerkin method

Lianyong Wei & Jun Zou✉

The computation of electric field in transcranial magnetic stimulation (TMS) is essentially a problem of gradient calculation for thin layers. This paper introduces a hybrid-order hybridizable discontinuous Galerkin finite element method (HDG-FEM) and systematically demonstrates its superiority in TMS computations. The discrete format of HDG-FEM employing hybrid orders for TMS is derived and, from a fundamental numerical principle perspective, this study provides the elucidation of why HDG-FEM exhibits superior gradient computation capabilities compared to the widely used CG-FEM. Furthermore, the exceptional performance of HDG-FEM in thin layer calculation is demonstrated on both modified head models and realistic head models, focusing on three aspects: calculation errors, utilization of hybrid order, and computational cost. For the calculation of E-field in thin-layer regions with parameter mutation, the L_∞ norm error of the first-order HDG-FEM with the same tetrahedral mesh is comparable to the L_∞ norm error of the second-order CG-FEM. The L_2 norm error of the same-order HDG-FEM is smaller than that of the same-order CG-FEM. By utilizing the hybrid order, HDG-FEM achieves a rapid reduction in errors of thin layers without a significant increase in the computational cost. This study transforms the three-dimensional TMS problem into a special two-dimensional problem for computation, reducing computational complexity from p^3 in three dimensions to p^2 in two dimensions, while achieving significantly higher accuracy compared to the commonly used CG-FEM. The utilization of hybrid orders in thin layers of the head demonstrates significant flexibility, making HDG-FEM a new alternative choice for TMS computations.

Keywords Continuous Galerkin finite element method (CG-FEM), Hybridizable discontinuous Galerkin finite element method (HDG-FEM), Hybrid order, Transcranial magnetic stimulation (TMS), Parameter mutation, Thin layer

Transcranial magnetic stimulation (TMS) has emerged as a rapidly developing medical method for treating depression, epilepsy, and other neurological diseases[1–3]. The first practical TMS device was introduced in 1985, utilizing a coil near the head to induce an electric field (E-field) in target areas[4]. Accurate E-field distribution within the head is crucial to avoid spurious stimulation and improve therapeutic efficacy[5]. However, there is currently no effective technical means to accurately measure the distribution of the intracranial E-field[6–8]. Researchers have aimed to predict E-field distribution within the human heads. Initial attempts used a simplified spherical shell model with an analytical solution[9]. However, the spherical shell model is insensitive to the conductivity distribution and cannot accurately represent the complexity of a realistic human head[9–11]. To achieve precise calculation results, numerical methods are necessary to simulate head structures that are more intricate than the spherical shell model[10].

The current mainstream numerical methods for solving the TMS E-field problem are CG-FEM and boundary element method (BEM). CG-FEM is the most widely utilized numerical simulation method for TMS, including the usage of both software platform (e.g., MagNet[12,13], COMSOL[14], ANSYS[15], SimNIBS[16]) and self-developed CG-FEM programs[17,18]. In recent years, BEM has also made significant progress in fine-scale head simulations. Sergey N. Makarov improved the computational speed of the BEM algorithm by 500 times compared to Ansys

Dept. of Electrical Engineering, Tsinghua University, Beijing 100084, China. ✉email: zoujun@tsinghua.edu.cn

and released an open-source software toolkit based on MATLAB[19,20]. Luis J. Gomez conducted a comparative analysis of the convergence and the relationship between element order and size in TMS calculations using CG-FEM and BEM[21]. Konstantin Weise studied the impact of meninges, which is a structure thinner than CSF, on E-field calculations using a mesh-adaptive BEM program, achieving a mesh resolution of 0.1 mm[22]. However, these studies all assume that the conductivity parameters of the head model are isotropic, which is not biologically plausible[19]. Moreover, unlike CG-FEM, which naturally adapts to anisotropic materials, BEM requires additional processing to handle anisotropic material problems, resulting in increased complexity in using BEM[19].

The calculation of the E-field in TMS is particularly well-suited for the application of hybrid-order algorithms. The primary reasons are as follows: First, the model used for TMS is derived from magnetic resonance imaging (MRI) scans, which inherently contain model inaccuracies due to the limited resolution. Typically, the resolution of these models at the current technical level is around 1 mm, while the cerebrospinal fluid (CSF) and meninges, which are the thinnest structures in the human head, also have a thickness of approximately 1 mm. These structures, despite their thinness, significantly influence the distribution of the electric field in the head[22]. Under such resolution and scale, performing secondary meshing on existing models may introduce unpredictable model errors, rendering the computational results meaningless. Therefore, the original mesh should be used during the calculations. Second, the various structures within the head model differ greatly in both size and electrical parameters. For instance, the CSF is the area with the highest conductivity in the head structure, with a conductivity approximately 100 times higher than that of the skull[23]. Third, in three-dimensional cases, whether through mesh refinement or increasing the order of elements, the computational load increases dramatically. For instance, when employing a high-performance computer, the computational time for CG-FEM with seven million elements using third order would exceed one day which become unacceptable[21]. Given the unique characteristics of the head models, the development of new *p*-adaptive methods has emerged as a new choice.

The discontinuous Galerkin finite element method (DG-FEM), first proposed in 1973[24], is a numerical method that combines the CG-FEM and finite volume method (FVM). DG-FEM achieves complete decoupling between elements, allowing for natural use of unstructured meshes or hybrid-order elements, and seamless adaptation to anisotropic material parameters. The flexibility of DG-FEM in utilizing hybrid-order or unstructured meshes is particularly suited for solving the E-field distribution in realistic head models with complex thin layer structures.

The element conservation property of DG-FEM can mitigate the computational errors caused by model inaccuracies[25]. The governing equations of TMS satisfy the condition that the divergence to the current density is equal to zero[18]. CG-FEM only guarantees global flux conservation, whereas DG-FEM ensures flux conservation at the element level. This element conservation property of DG-FEM allows it to effectively avoid the "skull leakage effect" which may occur in computations using CG-FEM[25,26].

The TMS pays focuses on the local E-field distribution due to its stimulation occurring at the cellular level. The induced E-fields associated with TMS have a complex and often counter-intuitive spatial distribution, which is dependent on the individual anatomy of a target subject[11,27]. Different numerical methods differ in the maximum value of the E-field when using the same head model as in Ref.[28], which highlights the importance of numerical method reliability. DG-FEM and CG-FEM employ distinct gradient solving mechanisms to ensure the accuracy of DG-FEM gradients throughout the solution process[26].

Recently, an improved numerical method known as HDG-FEM has emerged and gained popularity because it reduces the degrees of freedom (DOF) of the traditional DG-FEM while retaining all of its original advantages[29–31]. To the best of the authors' knowledge, there is currently no publicly available DG-FEM using *p*-adaptivity for TMS research. In this study, the HDG-FEM using hybrid order is introduced to solve the head E-field calculation problems of TMS. HDG-FEM's excellent ability to handle complex head geometries and large differences in electrical parameters will be fully utilized. The paper is organized as follows: In Section II and the Supplementary Material, the discrete formulation of HDG-FEM for the governing equations of TMS is derived, and the strong gradient computation capability of HDG-FEM is explained from a numerical principle perspective, which demonstrate the necessity of introducing HDG-FEM. In Section III and IV, the superior TMS solving capability of HDG-FEM is demonstrated using a modified sphere model and a realistic head model, focusing on E-field error, application of hybrid-order elements, and computational cost. The approach involves initially validating the algorithm's performance on a simple model before transitioning to more complex head models. Finally, the conclusions of this paper are presented.

Theory and method

Typically, the frequency of pulse currents in TMS is below 10 kHz, allowing displacement currents to be neglected and enabling the TMS calculation to be treated as a quasi-static magnetic field problem[18,20,32,33]. Furthermore, reference[33] indicates that TMS calculations pertain to low-frequency, low-conductivity scenarios, permitting the separation of the head and surrounding air regions and confining the solution domain to within the head.

The governing equations

To focus the research question, the solution domain of this study is limited to the entire head. As illustrated in Fig. 1, the current and E-field are induced on the inner side of the head under the stimulation of time-varying current in the coils. V_1 and V_2 denote regions within the head with different material parameters. Thus, the entire solution domain Ω can be represented by:

$$\begin{aligned} \Omega &= V_1 \cup V_2 \cup V_i \\ \partial\Omega &= \Gamma_N \cup \Gamma_D \\ \Gamma_{12} &= \partial V_1 \cap \partial V_2 \end{aligned} \tag{1}$$

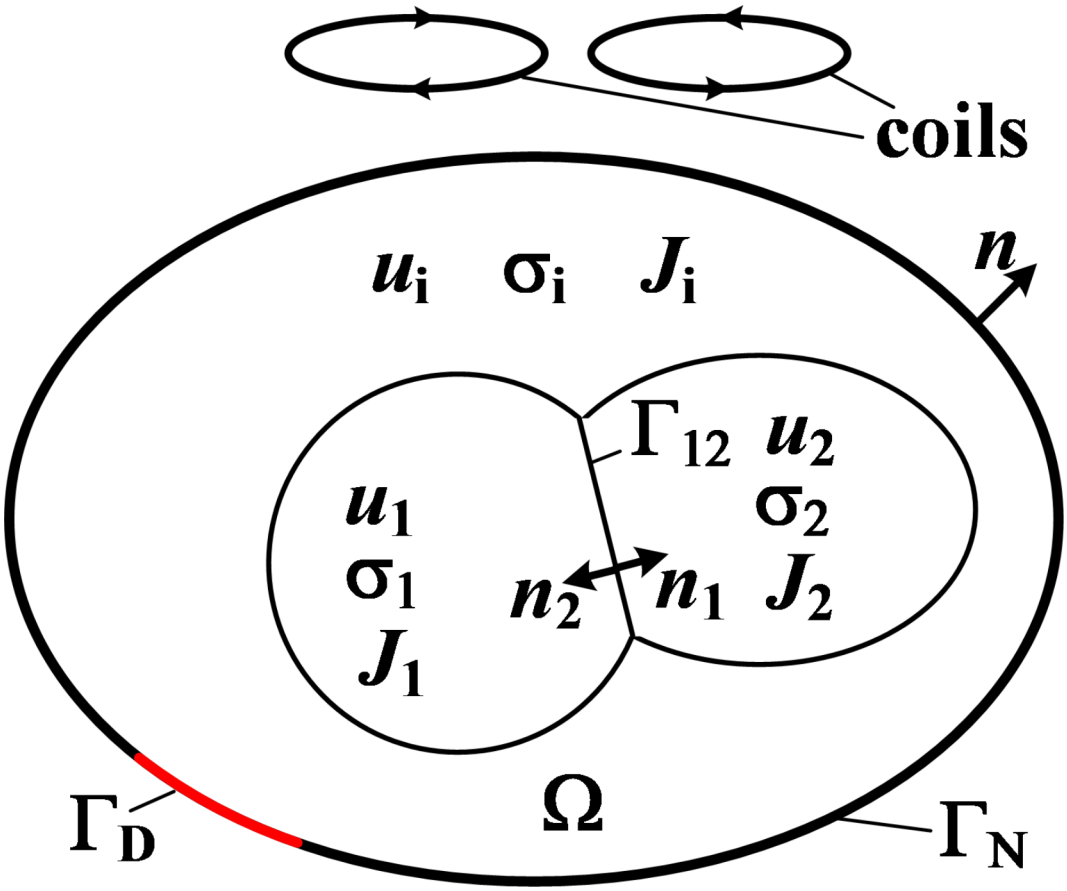

Fig. 1. Schematic diagram of distinct regions in the solution domain.

where $\partial\Omega$ denotes the boundary of the entire solution region. Γ_D represents the Dirichlet boundary, Γ_N represents the Neumann boundary surface. And Γ_{12} represents the internal interfaces.

The E-field intensity $\boldsymbol{E}$ and current density $\boldsymbol{J}$ can be calculated using the following formulas[18,34]:

$$\begin{aligned} \mathbf{E} &= -\nabla u - \frac{\partial \mathbf{A}}{\partial t} \\ \mathbf{J} &= \sigma \mathbf{E} = \begin{bmatrix} \sigma_{xx} & \sigma_{xy} & \sigma_{xz} \\ \sigma_{yx} & \sigma_{yy} & \sigma_{yz} \\ \sigma_{zx} & \sigma_{zy} & \sigma_{zz} \end{bmatrix} \left(-\nabla u - \frac{\partial \mathbf{A}}{\partial t} \right) \end{aligned} \tag{2}$$

where $\boldsymbol{A}$ is the magnetic vector potential within the solution region; u is the scalar potential and $\boldsymbol{\sigma}$ is the conductivity tensor. In the case of low frequency and low conductivity, the magnetic vector potential generated by eddy currents in biological tissues is much smaller than that produced by the coil. Hence, the coils' magnetic vector potential can be substituted for that of the biological tissues, achieving decoupling of the scalar potential and magnetic vector potential[33]. In this study, the magnetic vector potential $\boldsymbol{A}$ of the coil is assumed to be known and has been pre-computed.

The normal directions of the current density $\boldsymbol{J}$ are continuous at the interfaces of different materials. Because the conductivity of air is zero, the normal component of the current density $\boldsymbol{J}$ is zero at the interface between air and scalp[33,34]. It is assumed that the conductivity of each structure within the solution domain is constant. Based on the current continuity law and (2), the form of the governing equation of TMS used for HDG-FEM can be written as follows:

$$\begin{cases} -\nabla \cdot \left(\sigma \left(\nabla u + \dfrac{\partial \mathbf{A}}{\partial t} \right) \right) = 0 \quad \text{in } \Omega \\ \sigma_1 \left(\dfrac{\partial u}{\partial n_1} + \mathbf{n}_1 \cdot \left(\dfrac{\partial \mathbf{A}}{\partial t} \right) \right) + \sigma_2 \left(\dfrac{\partial u}{\partial n_2} + \mathbf{n}_2 \cdot \left(\dfrac{\partial \mathbf{A}}{\partial t} \right) \right) = 0 \quad \text{on } \Gamma_{12} \\ \sigma_i \dfrac{\partial u}{\partial n} = -\mathbf{n} \cdot \left(\sigma_i \dfrac{\partial \mathbf{A}}{\partial t} \right) \quad \text{on } \Gamma_N \end{cases} \tag{3}$$

where $\boldsymbol{n}_1$ and $\boldsymbol{n}_2$ are the normal vectors of the interfaces in Fig. 1.

It should be noted that the governing equation of TMS is an eddy current field equation. Its interface conditions must be strictly satisfied in Eq. (3). In fact, all boundaries are Neumann boundaries in TMS. To make (3) have a unique solution, it is also necessary to set a Dirichlet boundary condition. In fact, TMS focuses on the gradient of u, i.e., the E-field value, rather than the value of u itself. The simplest approach is to select any point in the solution domain and set the value of u to a known value.

The weak form of HDG-FEM

To secure geometric flexibility and pave the way for the HDG-FEM formulation, we assume that the solution domain can be partitioned and approximated using K elements, that is:

$$\Omega \simeq \Omega_h = \bigcup_{e=1}^{K} \Omega_e,\ \Omega_i \cap \Omega_j = \emptyset\ for\ i \neq j \tag{4}$$

If $\partial\Omega_i$ is used to represent the surface of the i-th element, then Γ can be defined as follows:

$$\Gamma := \left[\bigcup_{e=1}^{K} \partial\Omega_e\right] \backslash \partial\Omega \tag{5}$$

Following the HDG-FEM rationale, the governing equation of TMS is divided into two parts: a local problem and a global problem; Correspondingly, HDG-FEM solves the local problem and global problem respectively. As shown in Fig. 2, HDG-FEM defines three faces on each interface: the interior face, the exterior face, and the virtual face. Typically, the element currently being analyzed is denoted as '$\boldsymbol{e}^-$', while the adjacent element is denoted as '$\boldsymbol{e}^+$'. And the superscript "$-$" represents the interior face of the element; The superscript "$+$" represents the exterior face of the adjacent element. The local problem addresses the relationship between quantities inside the element and those on the virtual face, while the global problem resolves the relationships among all virtual face quantities. Unlike traditional DG methods, HDG-FEM explicitly solves for the quantities on the virtual face.

First, a new mixed variable $\boldsymbol{q} = -\nabla u$ is introduced, and the governing equation is rewritten into multiple first-order equations in each element[30,31]. As illustrated in Fig. 2, the solution of HDG-FEM at the intersection points inherently contains discontinuities, which can be denoted as u^+ and u^-. To express the unique value of the solution at the intersection points, i.e., the trace of the solution at the virtual face, HDG-FEM introduces an independent hybrid variable $\hat{u}$. In other words, a virtual face is added on each real interface, and the hybrid variable $\hat{u}$ is the quantity to be solved on the virtual face. The purpose of the local problem equation is to establish the relationship between the nodal values of u^- (i.e., u) and $\hat{u}$ on the element Ω_e. And the equations of the local problem are as follows:

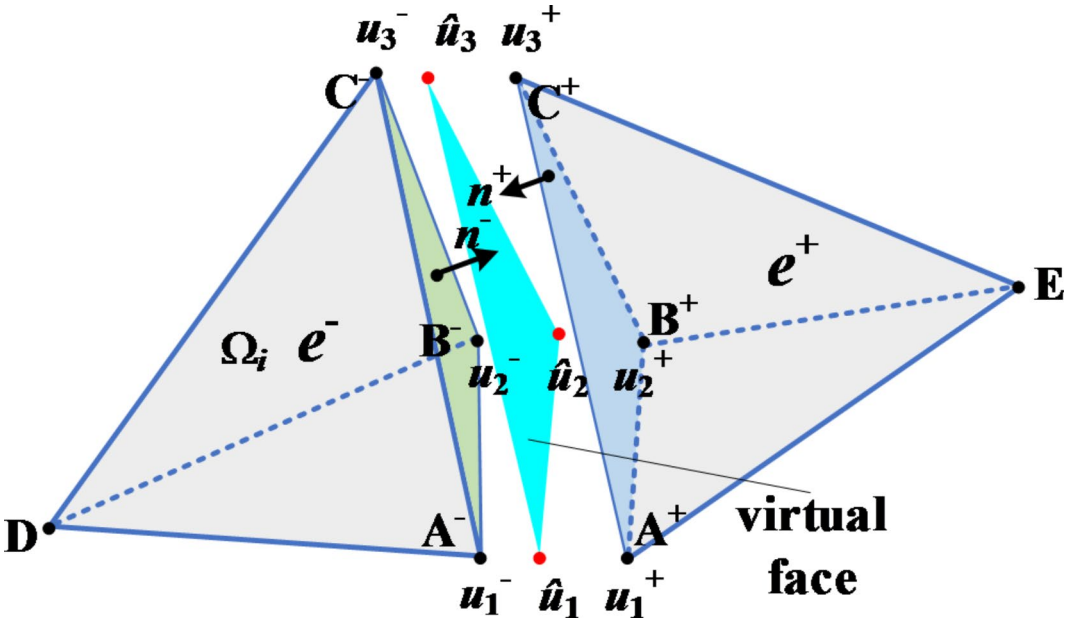

Fig. 2. Illustration of the three surfaces and associated variables set at the interface between two adjacent elements in HDG-FEM.

$$\begin{cases} \mathbf{q}_e = -\nabla u_e \quad \text{in } \Omega_e \\ \nabla \cdot (\sigma \mathbf{q}_e) = \nabla \cdot \left(\sigma \dfrac{\partial \mathbf{A}}{\partial t} \right) \text{ in } \Omega_e \\ u_e = u_D \quad \text{on } \partial\Omega_e \cap \Gamma_D \\ u_e = \hat{u} \quad \text{on } \partial\Omega_e \backslash \Gamma_D \end{cases} \tag{6}$$

Second, the purpose of the global problem is to establish connections between different mesh elements. And the hybrid variable (i.e., the global variable) $\hat{u}$ is determined in the global problem. Based on the transmission conditions on the internal interfaces and Neumann boundary, the global problem can be obtained as follows:

$$\begin{cases} [\![u\boldsymbol{n}]\!] = 0 \quad \text{on } \Gamma \\ \left[\!\left[\boldsymbol{n} \cdot \sigma \left(\mathbf{q} - \dfrac{\partial \mathbf{A}}{\partial t} \right) \right]\!\right] = 0 \text{ on } \Gamma \\ \boldsymbol{n} \cdot \sigma \boldsymbol{q} = \boldsymbol{n} \cdot \sigma \dfrac{\partial \mathbf{A}}{\partial t} \quad \text{on } \Gamma_N \end{cases} \tag{7}$$

where $[[\cdot]]$ is a jump operator, and it is defined as:

$$[[s]] = \mathbf{n}^- s^- + \mathbf{n}^+ s^+, \ [[\mathbf{s}]] = \mathbf{n}^- \cdot \mathbf{s}^- + \mathbf{n}^+ \cdot \mathbf{s}^+. \tag{8}$$

the variables "s" and "$\boldsymbol{s}$" in (8) respectively denote an arbitrary scalar and an arbitrary vector, $\boldsymbol{n}$ is the normal vector of the interface in Fig. 2. It is defined differently depending on whether the operand is a scalar or vector.

This paper conducts the analyses based on nodal HDG-FEM. In the discrete spaces V^h and $\hat{\boldsymbol{\mathcal{V}}}^h$ which are defined in[31], the primal mixed (u^{h}, $\boldsymbol{q}^{\mathrm{h}}$) and hybrid variables $\hat{u}$ can be represented by the following expressions:

$$u^h = \sum_{i=1}^{np} N_i u_i, \ \mathbf{q}^h = \sum_{i=1}^{np} N_i \mathbf{q}_i, \ \hat{u}^h = \sum_{i=1}^{nfp} \hat{N}_i \hat{u}_i \tag{9}$$

where np and nfp are the total number of interpolation points of p-order polynomial on the element and element face, respectively. N_i and $\hat{\mathrm{N}}_{\mathrm{i}}$ are the shape functions defined on the reference element and the reference face, respectively. The subscript i indicates the i-th node.

An important challenge in using the hybrid-order HDG-FEM is to determine the order of the hybrid variable $\hat{u}$ at the virtual face in Fig. 2. A tetrahedron has four faces, which means that an element needs to determine the orders of the four $\hat{u}$ variables at the virtual faces between four adjacent elements. Specifically, if a shared mesh face is a boundary surface, the order of the face is equal to the order of the element. Otherwise, if the shared mesh face is an interior face, the order of the face is equal to the maximum order of the two adjacent elements. Thus, the order of variable $\hat{u}$ at any virtual face can be calculated using the following formula:

$$p_f = \begin{cases} p \quad \text{on } \Gamma_{\mathrm{N}} \\ \max\{p(e^-), p(e^+)\} \text{ on } \Gamma \end{cases} \tag{10}$$

where e^- and e^+ represent the current element and its adjacent element, respectively. Note that p represents the order of each volume element, whereas p_{f} represents the order of the virtual faces.

To obtain the weak form of the local problem in (6), we need to find $\left(u_e^h, \ \boldsymbol{q}_e^h\right) \in \mathrm{V}^h(\Omega_e) \times [\mathrm{V}^h(\Omega_e)]^{nsd}$ for $e = 1,2,3\ldots K$ that satisfies:

$$\begin{cases} -\left(\boldsymbol{w}, \boldsymbol{q}_e^h\right)_{\boldsymbol{\Omega}_e} + \left(\nabla \cdot \boldsymbol{w}, u_e^h\right)_{\boldsymbol{\Omega}_e} = \langle \boldsymbol{n} \cdot \boldsymbol{w}, u_D \rangle_{\partial \boldsymbol{\Omega}_e \cap \boldsymbol{\Gamma}_D} + \left\langle \boldsymbol{n} \cdot \boldsymbol{w}, \hat{u}^h \right\rangle_{\partial \boldsymbol{\Omega}_e \backslash \boldsymbol{\Gamma}_D} \\ \left(v, \nabla \cdot (\sigma \boldsymbol{q}_e^h)\right)_{\boldsymbol{\Omega}_e} + \left\langle v, \tau\sigma u_e^h \right\rangle_{\partial \boldsymbol{\Omega}_e} = \langle v, \tau\sigma u_D \rangle_{\partial \boldsymbol{\Omega}_e \cap \boldsymbol{\Gamma}_D} + \left\langle v, \tau\sigma \hat{u}^h \right\rangle_{\partial \boldsymbol{\Omega}_e \backslash \boldsymbol{\Gamma}_D} + (v, \nabla \cdot (\sigma \dfrac{\partial \mathbf{A}}{\partial t}))_{\boldsymbol{\Omega}_e} \end{cases} \tag{11}$$

where $(\boldsymbol{w}, v) \in [\mathrm{V}^h(\Omega_e)]^{nsd} \times \mathrm{V}^h(\Omega_e)$. In practice, $(\boldsymbol{w}, v)$ is typically replaced directly by the shape functions in (9). And nsd is the dimension of the solution domain. The symbol $(\cdot, \cdot)$ indicates the inner product whose integral region is in element Ω_e. whereas the symbol $<\cdot, \cdot>$ indicates the inner product whose integral region is on the surfaces of Ω_e. The stability parameter τ is chosen as a constant in this study[29].

The integration of (11) solely involves the interior of each element and the newly introduced traces $\hat{u}$ in Fig. 2, establishing no connection with neighboring elements. And the order of each element in HDG-FEM is independent of the order of the adjacent elements, allowing them to be unequal. This characteristic makes the adoption of the hybrid order in HDG-FEM a natural choice.

Similarly, the weak form of the HDG-FEM global problem is to find $\widehat{u} \in \hat{\boldsymbol{\mathcal{V}}}^h(\Gamma \cup \Gamma_{\mathrm{N}})$ that satisfies:

$$\sum_{e=1}^{K} \left\{ \left\langle \hat{v}, n \cdot \sigma (q_e^h - \frac{\partial \mathbf{A}}{\partial t} \right\rangle_{\partial \Omega_e \backslash \Gamma_D} + \left\langle \hat{v}, \tau\sigma u_e^h \right\rangle_{\partial \Omega_e \backslash \Gamma_D} - \left\langle \hat{v}, \tau\sigma \hat{u}^h \right\rangle_{\partial \Omega_e \backslash \Gamma_D} \right\} = \sum_{e=1}^{K} \left\langle \hat{v}, \sigma \frac{\partial \mathbf{A}}{\partial t} \right\rangle_{\partial \Omega_e \cap \Gamma_N} \tag{12}$$

for all $\widehat{v}\in\hat{\boldsymbol{\mathcal{V}}}^h(\Gamma\cup\Gamma_N)$. In practice, $\widehat{v}$ is typically replaced directly by shape functions which is similar to the weak form of the local problem. Note that all integrals in (12) are surface integrals, indicating that the size of the global matrix is proportional to $(p+1)(p+2)/2$ in 2D, rather than $(p+1)(p+2)(p+3)/6$ in 3D of traditional DG methods. The introduction of HDG-FEM transforms the 3D TMS computational problem into a specialized 2D problem, reducing the growth rate of computational complexity from p^3 in three dimensions to p^2 in two dimensions when using high-order elements.

If the conductivity parameter is isotropic and constant, HDG can be written in a simple matrix format. For each element Ω_e, $e=1,2,3\ldots K$, rewriting the weak form of the local problem in (11) into the matrix form[31], one can get:

$$\begin{bmatrix} \sigma\mathbf{K}_{uu} & \sigma\mathbf{K}_{uq} \\ \mathbf{K}_{uq}^T & \mathbf{K}_{qq} \end{bmatrix} \begin{Bmatrix} \mathbf{u} \\ \mathbf{q} \end{Bmatrix}_e = \begin{Bmatrix} \sigma\mathbf{f}_u \\ \mathbf{f}_q \end{Bmatrix}_e + \begin{Bmatrix} \sigma\mathbf{K}_{u\hat{u}} \\ \mathbf{K}_{q\hat{u}} \end{Bmatrix}_e \hat{\mathbf{u}}_e \tag{13}$$

Similarly, the weak form of the global problem can be expressed in the following matrix form:

$$\sum_{e=1}^{K} \left\{ \begin{bmatrix} \sigma\mathbf{K}_{u\hat{u}}^T & \sigma\mathbf{K}_{q\hat{u}}^T \end{bmatrix}_e \begin{Bmatrix} \mathbf{u} \\ \mathbf{q} \end{Bmatrix} + [\sigma\mathbf{K}_{\hat{u}\hat{u}}]_e \hat{\mathbf{u}}_e \right\} = \sum_{e=1}^{K} \left\{ [\mathbf{f}_{\hat{u}}]_e + [\mathbf{f}_A]_e \right\} \tag{14}$$

By substituting (13) into (14), the matrix form of the HDG-FEM global problem for $\widehat{u}$ can be quickly obtained as follows:

$$\mathbf{K}\hat{\mathbf{u}} = \mathbf{b} \tag{15}$$

The implementation details of (6)–(15) are provided in the Supplementary Material. And the Supplemental Material also provides an analysis from the perspective of discrete scheme to further elucidate the fundamental distinctions between HDG-FEM and CG-FEM.

The necessity of introducing HDG-FEM

Once the value of $\hat{u}$ in (15) is solved, we can calculate the E-field intensity and current density element by element based on (13) and (2). In fact, (13) and (14) can be considered as three coupled first-order systems of equations with respect to u, $\boldsymbol{q}$, and $\hat{u}$. If the difficulty of solving the system is neglected, any one of u, $\boldsymbol{q}$, and $\hat{u}$ can be computed first. From this perspective, the HDG-FEM gradient variable $\boldsymbol{q}$, which corresponds to the E-field intensity in the study, can be directly computed. This fundamental difference from the scalar CG-FEM is noteworthy.

When solving boundary value problems using numerical methods, it is only possible to guarantee the satisfaction of either the "scalar potential function value continuity" or the "normal gradient continuity" condition. Fig. S1 in Supplementary Material illustrates the differences in mesh configurations between CG-FEM and HDG-FEM. In the case of CG-FEM, it chooses to ensure the "scalar potential function value continuity" while the continuity of the normal gradient is "implicitly assumed" (in reality, the continuity of the normal gradient is not satisfied). On the other hand, HDG-FEM chooses to ensure the "normal gradient continuity" while sacrificing the "scalar potential function value continuity". In a word, the discrete scheme of HDG-FEM ensures the continuous normality of current density, thereby guaranteeing the accuracy of nodal values through gradient calculations. In contrast, the residual in CG-FEM within the Galerkin weighted residual method reflects only the errors in nodal values, relying on the correctness of the nodal value calculations to ensure the accuracy of gradient calculations. This choice results in HDG-FEM having a stronger gradient calculation capability compared to CG-FEM. More details are provided in the Supplementary Material.

From the perspective of flux conservation, the governing equation for TMS can be expressed as $\nabla\cdot\boldsymbol{J}=0$. The continuity property of the normal current density in HDG-FEM ensures that all elements satisfy flux conservation, i.e., local flux conservation. Whereas CG-FEM only satisfies global flux conservation. Specifically, HDG-FEM can satisfy the TMS governing equation in an integral sense on each element, whereas CG-FEM can only satisfy it in a global sense. This local flux conservation property makes HDG-FEM inherently more suitable for computing the E-field in TMS for which highly emphasizes the accuracy of local E-field calculation.

The distinctive characteristics of HDG-FEM are expected to demonstrate superior performance compared to CG-FEM when computing E-field in thin-layer structures, particularly in the computation of E-field in regions such as CSF in the head. Additionally, HDG-FEM enables the utilization of higher-order meshes in critical regions such as CSF, while employing lower-order meshes in other areas, thereby significantly reducing mesh dependency and achieving a balance between computational efficiency and accuracy.

Solution settings

The HDG-FEM simulation results will be employed for comparative purposes with CG-FEM simulation results using an identical mesh. COMSOL Multiphysics is a commercial software based on CG-FEM, and its accuracy has been widely recognized[35]. The HDG-FEM simulation employs a tetrahedral mesh partitioned by COMSOL software. The governing equations in this study are solved using COMSOL's PDE module and its built-in solver. As a mature commercial software, we consider the solution results and computational time of COMSOL as a reference for evaluating the performance of CG-FEM.

HDG-FEM is implemented using MATLAB. The computing platform is a computer with a 64-bit operation system and 96 GB of Random Access Memory (RAM), and its processor is AMD EPYC 7551P 32-Core Processor CPU @ 2.00 GHz.

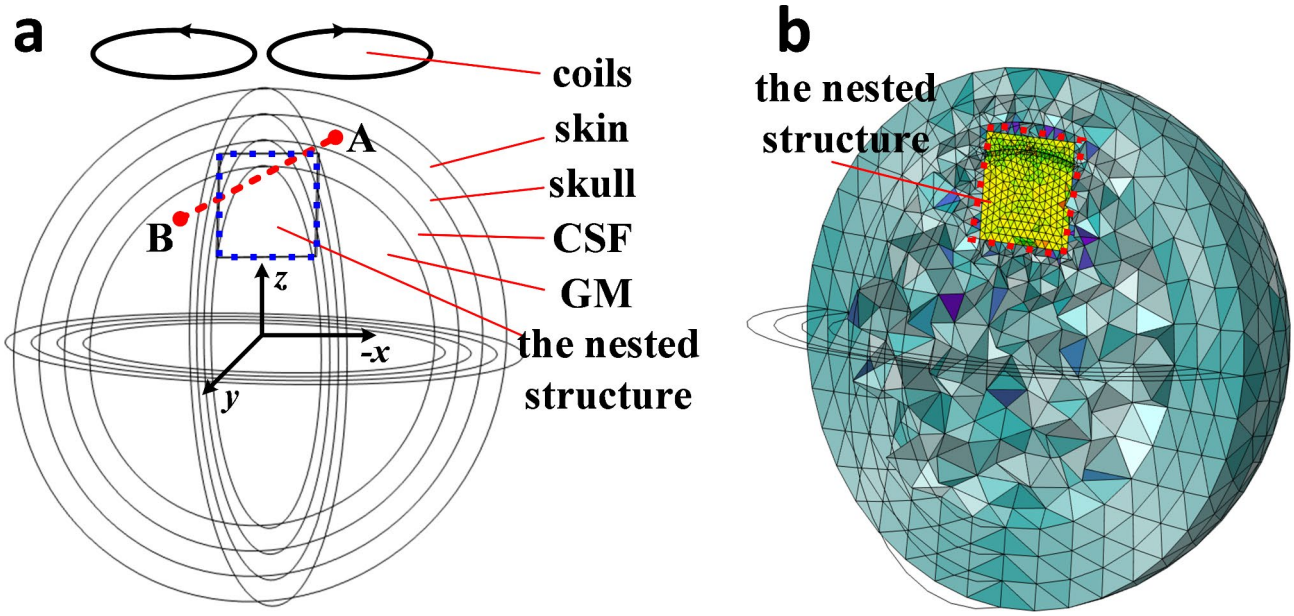

Fig. 3. The modified sphere model with a nested structure. **a** Geometric structure diagram of the TMS example. **b** Mesh partitioning.

Tissues	Skin	Skull	CSF	GM	WM	Cerebellum
σ (S/m)	0.148	0.0179	1.88	0.419	0.348	0.577

Table 1. Conductivity parameters of various tissues in the head[23].

The selection of the solvers is an essential part of the HDG-FEM algorithm. In this study, an algebraic multigrid (AMG) preconditioned iterative solver is employed to address the global problem of HDG-FEM. The CG method is accelerated by a classic AMG preconditioner. The convergence criterion for (15) is achieved when the relative residual error becomes smaller than the designated tolerance limit ε, and its expression is:

$$\frac{\left\|\mathbf{b}-\mathbf{A}\hat{\mathbf{u}}^{(k)}\right\|}{\|\mathbf{b}\|} \leqslant \varepsilon \tag{16}$$

where k is the number of iterations and $\|\cdot\|$ is the operation symbol for calculating the norm of a vector. The relative residual error ε is set to 10^{-7} in this study.

Analysis of a modified sphere model case

As a common practice, this section validates the algorithm's performance using a simplified model and prepares for its application in more complex realistic head models in the subsequent section. In this section, an example of TMS with modified sphere model is presented to illustrate the superiority of HDG-FEM in TMS calculation from three perspectives: E-field curves in thin layer, E-field calculation error.

Model and calculation details

The commonly used multi-layer spherical model structure does not involve the issue of drastic variations in the E-field in thin layers, which does not align with the E-field distribution characteristics of a realistic head model[9]. The complex nesting relationship between gray matter (GM) and CSF, along with the sudden change in conductivity, leads to the accumulation of charge in the elements, resulting in a complex distribution of the E-field. Note that the nested structures are thin layers.

To validate the computational capability of HDG-FEM in handling E-field calculation issues of thin layers, the commonly used homogeneous multi-layered sphere model is modified as shown in Fig. 3. It is important to note that Fig. 3 can be generated by adding the necessary annotations to the image exported from COMSOL. The first four layers of the sphere model correspond to the skin, skull, CSF, and GM, with radii of 0.1 m, 0.09 m, 0.08 m, and 0.07 m, respectively. The entire nested structure has dimensions of 0.04 m × 0.04 m × 0.002 m, with its center located at (0, 0, 0.055) m. The material parameters for the four-layer head model are listed in Table 1 which is the latest head electrical parameters[23], and the electrical conductivity of the nested structure is the same as that of the GM. This nested structure aims to simulate the impact of the mutual nesting of different tissues in a realistic head model on the computational results. The excitation source consists of two circular

loops forming a figure-of-eight (FOE) coil. The radius of each loop is 0.04 m, and they are parallel to the *xy* plane with their centers located at (±0.043, 0, 0.105) m. $\partial A/\partial t$ consists of spatial and temporal terms. The current amplitude of a single circular loop of the FOE coil is 10,000 A, with a time rate of change of $2\pi\times10^4$/s, corresponding to a frequency of 10 kHz. In view of the fact that the spatial magnetic vector potential of a circular coil can be analytically computed[33], this study models the whole head region without taking into account the air surrounding the head and the coil. The entire scalp surface is set as a Neumann boundary, and the lowest mesh face located at the bottom of the head is selected as a Dirichlet boundary with $u=0$.

E-field calculation in thin layers

All the curves in Fig. 4 represent the distribution of E-field norm along a line segment from point A (0.01, −0.04, 0.074) to point B (0.01, 0.04, 0.74). This line segment passes through the nested structure of the modified spherical model and can be considered as a representative segment. And the nested structure can be regarded as a thin layer. Note that "4 mm", "1 mm", "0.3 mm" refers to the size of the maximum tetrahedral mesh in the nested structure. Except for the nested structure, the maximum grid size of the mesh in other regions is consistently set to 0.02 m. Throughout the entire solving process, both HDG-FEM and CG-FEM adopt the same tetrahedral mesh structure.

As a comparison, the computational capability of CG-FEM in calculating E-field within a thin layer with parameter mutation is first evaluated. In Fig. 4, the 'Ref' curve represents the solution obtained using the CG-FEM with third-order elements and a "*p*-refinement" mesh refinement operation in COMSOL, which can be considered as an accurate solution. In Fig. 4a, there are always some discontinuities in the E-field norm obtained using first-order elements, resulting in jumps in the amplitude. This phenomenon is caused by the use of CG-FEM for solving, where each grid node on the element surface has two unequal E-field values. This numerical characteristic can lead to significant errors in the CG-FEM solution for thin layers with rapid parameter variation. For example, in Fig. 4a, the "1st CG 4 mm" curve exhibits a large jump in amplitude from 122 V/m to 188 V/m in the region of rapid E-field variation within the nested structure. This discrepancy is caused by insufficient refinement of the maximum grid size of 4 mm, leading to a significant deviation from the reference value. To obtain an accurate solution using CG-FEM, the maximum grid size of the nested structure needs to be refined from 4 mm to 0.3 mm. At this point, the number of elements in the grid increases from 25,469 to 1,969,599, resulting in a 77-fold increase in the grid quantity. A large number of elements are required when using first-order CG-FEM to solve E-field problems of thin layer with electrical parameter mutation, which is consistent with the conclusion in[21].

Second, the computational capabilities of HDG-FEM and CG-FEM in solving the E-field within a thin layer are compared under the same tetrahedral mesh. In Fig. 4b, a deliberately coarse mesh, consisting of 25,469 tetrahedral elements, same as the '1st CG 4 mm' mesh in Fig. 4a, is selected for testing purposes. On the left of the thin layer with parameter mutation, the maximum E-field values obtained using first-order HDG-FEM and second-order CG-FEM are 209 V/m and 179 V/m, respectively, whereas the accurate value is 199.8 V/m. The calculation errors for HDG-FEM and CG-FEM are 4.6% and 10.4%, respectively. On the right of the thin layer with parameter mutation, the maximum E-field values obtained using the first-order HDG-FEM and second-order CG-FEM are 202 V/m and 190 V/m, respectively. The calculation errors for HDG-FEM and CG-FEM are 1.1% and 4.9%, respectively. This indicates that first-order HDG-FEM exhibits higher computational accuracy than second-order CG-FEM in thin layer with parameter mutation. Further validation of this conclusion will be conducted by using a realistic head model.

Furthermore, the E-field convergence performance of HDG-FEM with hybrid order will be further analyzed in thin layer with parameter mutation. Figure 4c employs the same mesh as Fig. 4a. The mesh order in the nested structure varies from one to three, whereas the mesh order in other regions remains first-order. It can be observed that when the nested structure adopts second-order elements, the maximum value is approximately equal to the

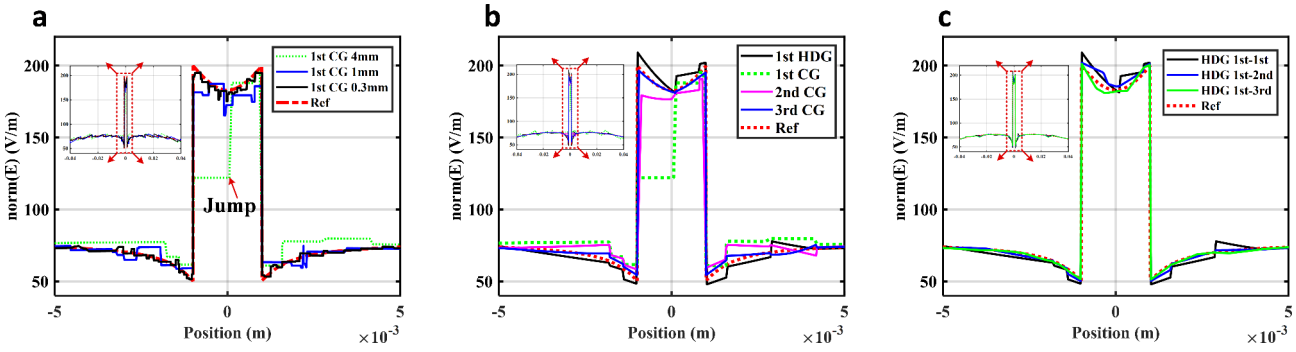

Fig. 4. Comparison of E-field norm curves on line segment AB which traversed through a thin layer structure under different configurations. **a** Solution results of CG-FEM using first-order elements with different element sizes. **b** Solution results of CG-FEM and HDG-FEM with different element orders but the same element size. **c** Solution results of HDG-FEM with hybrid order when the nested structure employs different element orders. Note that the regions of E-field mutation for all curves in the three subfigures are located within the nested structure.

reference solution. When the nested structure adopts third-order elements, the E-field norm curve overlaps closely with the reference solution. Using high-order grids in the nested structure region and low-order grids in other areas does not significantly increase the computational cost, as the nested structure grid only represents a small portion of the overall grid. In contrast, CG-FEM experiences a sharp increase in computational cost when using high-order grids or refining the mesh due to the inconvenience of utilizing hybrid-order grids.

Error analysis of hybrid order

In (17), three error metrics are defined to evaluate the E-field calculation capability of HDG-FEM in TMS: the maximum value error (L_{max}), infinity norm L_∞ error, the L_2 norm error, where '$\boldsymbol{E}_{ref}$' represents the reference solution. The L_{max} error and L_∞ reflect the computational capability of the E-field in capturing critical details within the biological tissue, whereas the L_2 norm error describes the overall error. The introduction of the maximum value error for the E-field magnitude is motivated not only by the high significance of the maximum field intensity in the coil design of TMS but also by the close correlation between the biological response of neural cells and the local maximum field intensity.

$$
\begin{aligned}
err_{L\max} &= abs\left(\frac{\max(||\mathbf{E}||) - \max(||\mathbf{E}_{ref}||)}{\max(||\mathbf{E}_{ref}||)}\right) \\
err_{L\infty} &= \frac{\max(||\mathbf{E} - \mathbf{E}_{ref}||)}{\max(||\mathbf{E}_{ref}||)} \\
err_{L2} &= \sqrt{\frac{\sum\int ||\mathbf{E} - \mathbf{E}_{ref}||^2 d\Omega_i}{\sum\int ||\mathbf{E}_{ref}||^2 d\Omega_i}}
\end{aligned}
\tag{17}
$$

Figure 5 quantifies the computational errors presented in Fig. 4. All curves in Fig. 5 utilize the same mesh as the '1st CG 4 mm' case in Fig. 4a. In Fig. 5a, the solid line represents the L_{max} error for the entire model, whereas the dashed line and discrete points both represent the L_{max} error within the nested structure. The maximum value of the E-field curve in Fig. 4 does not correspond to the maximum value of the E-field within the nested structure. First, concerning the solid line, it can be observed that the error for the first-order HDG-FEM is 2.67%, whereas the error for the second-order CG-FEM is 2.98%. The error of the first-order HDG-FEM is lower than that of the second-order CG-FEM. Regarding the computation error of E-field within the nested structure region, the first-order HDG-FEM exhibits an even lower error than the third-order method, demonstrating its exceptional E-field computation capability. Furthermore, adopting a hybrid-order strategy where higher-order elements are used in the nested structure region and lower-order elements are used in other regions can also effectively reduce L_∞ errors.

In Fig. 5a, the higher-order region only includes the nested structure, whereas in Fig. 5b, the higher-order region corresponds to the nested structure region and the entire CSF region. The reason for this change is that the nested structure occupies only a small volume in the modified spherical model, and the L_2 norm error is an integral quantity. Improving the accuracy of the local details does not significantly reduce the overall error. In Fig. 5b, the solid lines represent the errors when all elements use the same order, whereas dashed lines represent the error when a hybrid order is used. Overall, the L_2 errors of HDG-FEM with a single order are lower than

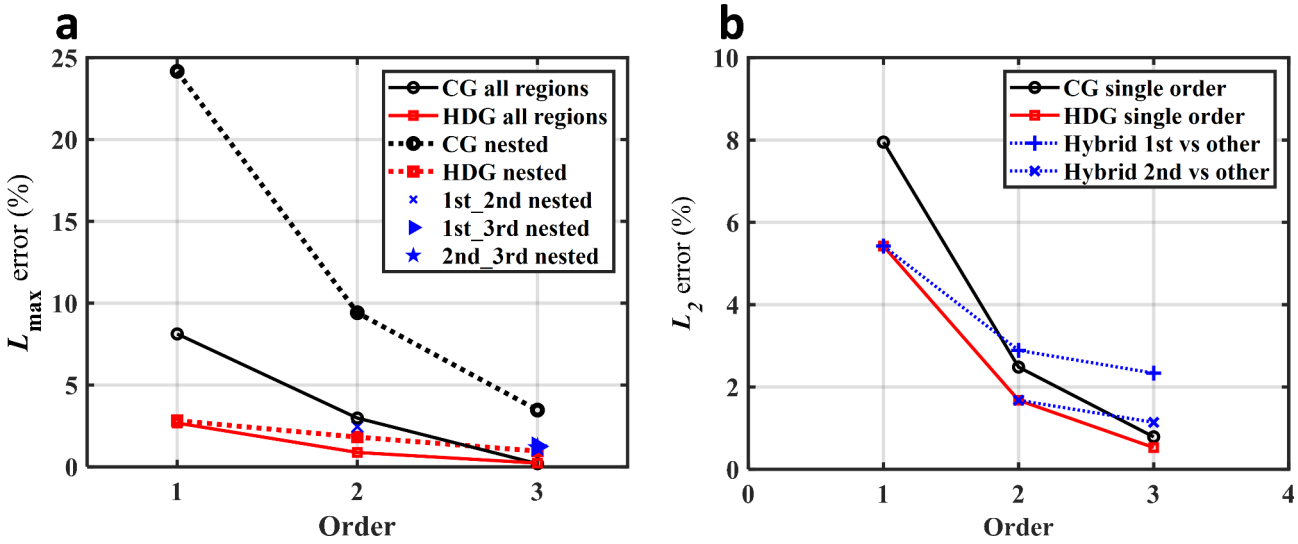

Fig. 5. Comparison curves of computational accuracy between HDG-FEM and CG-FEM for different element orders. **a** Variation curves of the maximum E-field value error in the entire modified spherical model region and the nested structure region. **b** Variation curves of the E-field L_2 norm in the entire modified spherical model region.

those of CG-FEM; for the case of hybrid orders, when the higher-order region has an order of 2nd and the lower-order region has an order of 1st, the L_2 error is 2.8%, while the error of CG-FEM using exclusively second-order elements is 2.4%, with no significant difference between the two; when using hybrid elements of first and third orders, the error of HDG-FEM is 2.3%, which is already lower than the error of second-order CG-FEM. In contrast, the errors of CG-FEM and HDG-FEM when using exclusively first-order elements are 7.9% and 5.4%, respectively. This indicates that using higher-order elements in critical regions (CSF and the nested structure regions) can achieve a rapid decrease in L_2 norm error. Owing to the significant differences in size and conductivity among different structures in the realistic heads, this hybrid-order strategy will have a noticeable effect on reducing errors when computing a realistic head model.

Realistic head model calculation

The section begins by analyzing the geometric structure and distribution characteristics of the electrical parameters in a realistic head model. Based on the aforementioned comparison results between HDG-FEM and CG-FEM, the advantages of HDG-FEM in solving a realistic head model are highlighted. The exceptional performance of HDG-FEM in solving realistic head models will be presented in the following aspects: solution settings, comparison of the errors between HDG-FEM and CG-FEM, solution DOF, and computational time. Finally, a relevant discussion on the computational results of this study is provided.

The head model and solution settings

The Population Head Model Repository offers mesh files of 50 human heads, each comprising seven parts: the skin, skull, CSF, GM, white matter (WM), cerebellum, and ventricle[36]. The conductivity of the last three parts, namely the WM, cerebellum, and ventricle, is similar to that of GM in Table 1, and they are generally at a considerable distance from the stimulation source. To emphasize the research focus and demonstrate the E-field calculation capability of HDG-FEM in thin layers with parameter mutation, deliberate disregard of the three structural components is implemented. Thus, this study concentrates on analyzing four parts: the skin, skull, CSF, and GM. The head model selected for this study corresponds to Model #101309 in Ref.[36].

In Fig. 6, the head region is divided into 2.33 million tetrahedral meshes. Similar to Figs. 3 and 6 can be directly exported from COMSOL and annotated as needed. As shown by the elliptical dashed line, many tiny and complex CSF structures are deeply nested in the GM. Refining these structures poses technical challenges while also significantly increasing mesh quantity. An unsuitable division of the tiny structures could easily lead to

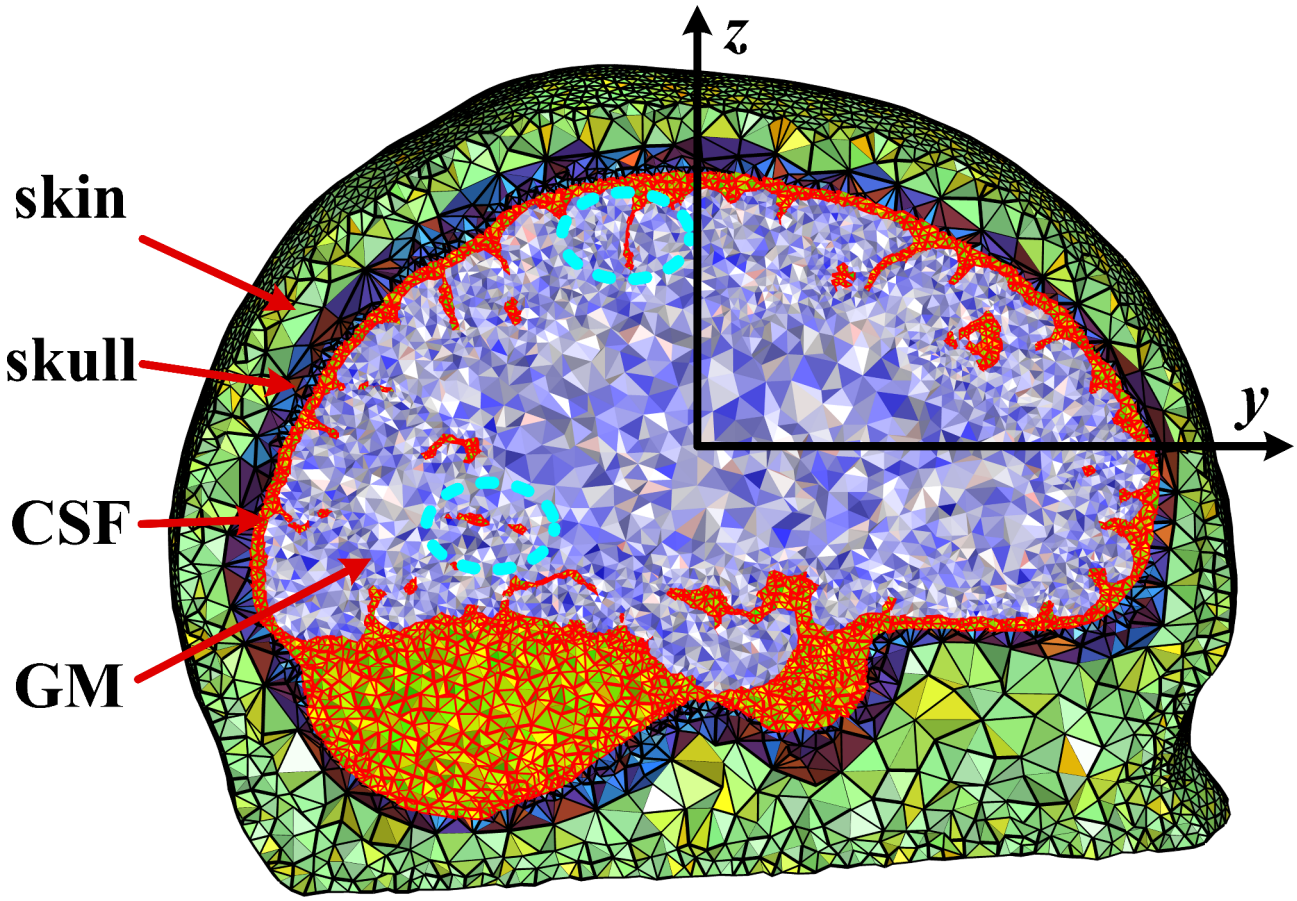

Fig. 6. Section of the head model mesh with thin layer structures.

inconsistencies to the biological structure. The inherent characteristics of the realistic head model naturally lend itself to the application of the hybrid order strategy in HDG-FEM. Given that CSF has the highest conductivity among all the structures and the conductivity difference between CSF and the skull and GM is significant, the precision of the calculation of the CSF E-field has a direct bearing on the precision of the entire head area E-field calculation.

The excitation source is a FOE coil. The mesh file (#101309) has a pre-defined spatial coordinate system, and the center of the FOE coil is located at the coordinates of ($\pm$0.043, 0, 0.11) m, with a radius of 0.04 m. The plane of the coil is parallel to the *xy* plane, and the current amplitude of a single circular loop of the FOE coil is 10,000 A, with a time rate of change of $2\pi\times10^4$/s.

Differences in solutions between HDG-FEM and CG-FEM

First, an intuitive analysis of the E-field solving capability of HDG-FEM in critical regions is presented. The skin surface of the head model is closest to the excitation source, while the GM is the main region where the E-field is biologically relevant, and the GM surface structure is more complex than the skull surface and CSF surface. Therefore, the scalp surface and GM surface are chosen as representatives for the analysis. Based on the 3D coordinates and values of all nodes from both CG-FEM and HDG-FEM, Fig. 7 can be plotted using MATLAB. In Fig. 7, the reference solution, which is represented by 'Ref', is obtained by solving with COMSOL with an average mesh size of 0.8 mm, approximately 50 million mesh elements, and second-order mesh elements. Based on the multiple simulations conducted in this study and the conclusions of[21], the reference solution can be considered as the exact solution. Figure 7 compares the errors between the first-order CG-FEM, second-order CG-FEM, first-order HDG-FEM, and reference solution. Overall, the errors are mainly concentrated in a small region directly below the FOE coil, whereas the errors in the other regions are approximately zero. Specifically, the maximum norm of the reference E-field on the skin surface is 82.7 V/m. The maximum E-field norms on the skin surface for the first-order CG-FEM, second-order CG-FEM, and first-order HDG-FEM are 71.3 V/m, 78.2 V/m, and 83.1 V/m, respectively. The maximum E-field norm errors are 11.3 V/m, 7.5 V/m, and 6.1 V/m, respectively. It can be observed that in terms of both the maximum E-field magnitude and the maximum E-field magnitude error, the first-order HDG-FEM outperforms the second-order CG-FEM. Similarly, the maximum norm of the reference E-field on the GM surface is 72.8 V/m. The maximum E-field norms on the GM surface for the first-order CG-FEM, second-order CG-FEM, and first-order HDG-FEM are 50.4 V/m, 57.2 V/m, and 74.1 V/m, respectively. The maximum E-field norm errors are 28.5 V/m, 15.2 V/m, and 11.9 V/m, respectively. The same conclusion can be drawn for the GM surface as for the skin surface, indicating that the first-order HDG-FEM exhibits a superior capability in calculating the maximum E-field compared to the second-order CG-FEM.

Second, the quantification results of the errors in the realistic head model can be summarized in three aspects: HDG-FEM exhibits excellent capability in solving the maximum E-field values, the first-order HDG-FEM has a lower L_∞ norm error than the second-order CG-FEM, and the L_2 norm error of the same-order HDG-FEM is lower than that of CG-FEM. In Fig. 8, the errors of the results in Fig. 7 are further quantified. Regarding the element order, the use of fourth-order elements in HDG-FEM and CG-FEM leads to a sharp increase in the number of variables and required memory, as well as a deterioration in matrix sparsity. This makes computing using general-purpose platforms challenging. Therefore, the highest element order for the mesh is set to third-order. Regarding the mesh size, according to the conclusions in[21], the average element sizes of the involved meshes are approximately 2.3 mm, 1.8 mm, 1.3 mm, and 0.8 mm, spanning the thresholds of 2 mm and 1 mm. The corresponding numbers of mesh elements are 2.33 million, 4.51 million, 10.74 million, and 50.82 million. In Fig. 8, the horizontal axis represents different mesh order settings, while the vertical axis indicates various types of errors. As shown in Fig. 8a, with an average mesh size of 2.3 mm, the maximum E-field norm (L_{max}) errors on

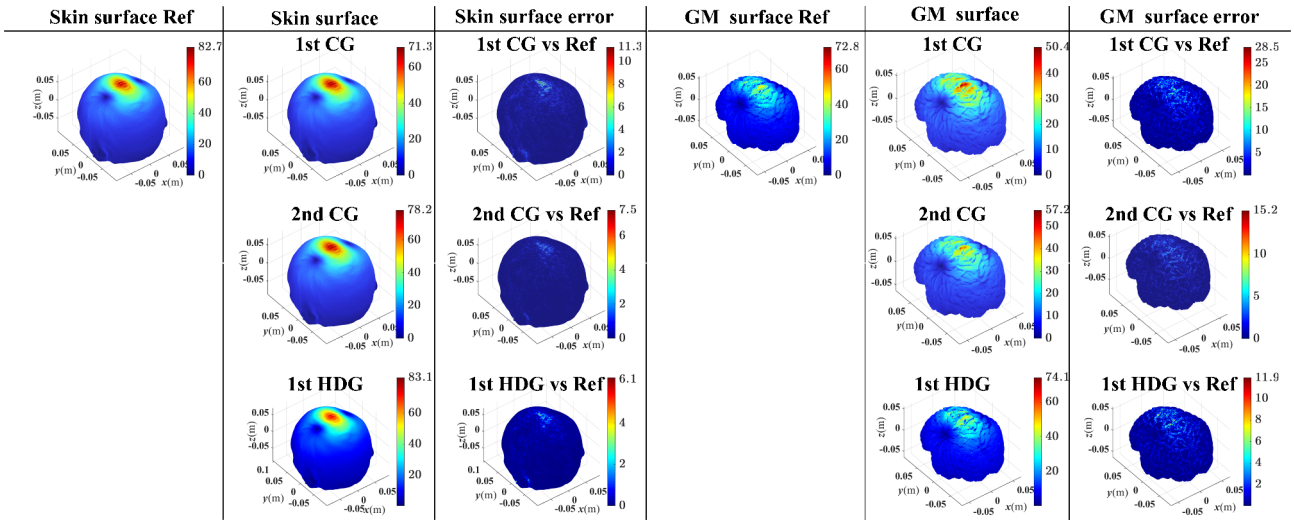

Fig. 7. Comparison of E-field distributions on the skin surface and GM surface obtained by HDG-FEM and CG-FEM on a mesh consisting of 2.33 million tetrahedral elements.

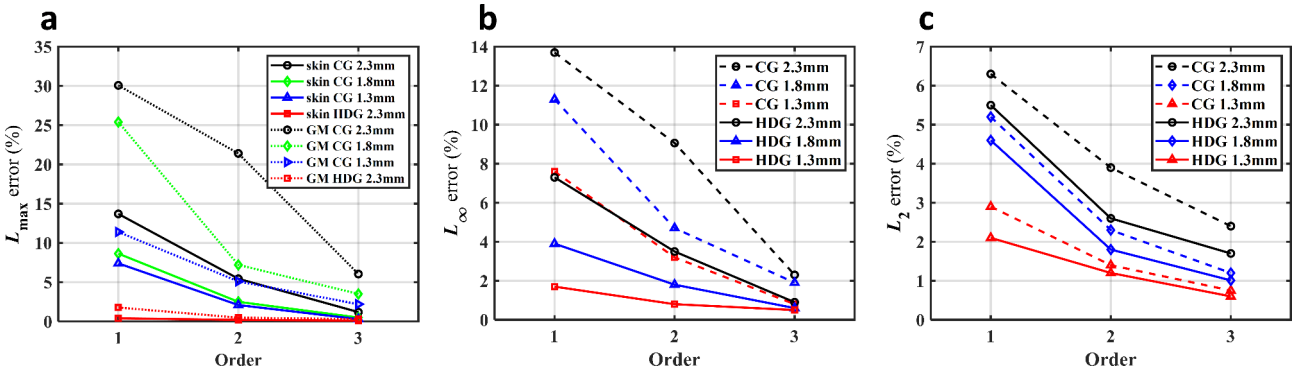

Fig. 8. Error curves of the E-field norm for HDG-FEM and CG-FEM under different mesh order settings. **a** Maximum E-field norm error L_{max} on the skin surface and GM surface. **b** L_∞ error on the GM surface. **c** L_2 error of the entire model.

Hybrid order	Skin	Skull	CSF	GM	Global
1_1_1_1	5.54	5.74	6.78	5.29	5.64
1_1_2_1	5.51	5.21	2.73	3.99	4.86
1_1_3_1	5.40	4.11	0.79	3.62	4.27
1_2_1_1	5.06	3.97	6.50	4.55	4.76
1_2_2_1	4.84	3.02	2.40	3.99	3.93
2_1_1_1	3.49	4.45	6.70	5.10	4.39
2_1_2_1	3.21	3.81	2.44	3.99	3.49
2_2_1_1	2.98	3.32	5.69	4.55	3.65
2_2_2_1	2.93	2.62	1.91	3.99	2.99
2_2_2_2	2.93	2.30	1.85	2.94	2.66
3_3_3_3	2.58	1.62	0.76	0.66	1.74

Table 2. The L_2 error percentages of different structures in the head using the hybrid-order HDG-FEM on a mesh with an average element size of 2.3 mm.

the skin and GM surfaces for the first-order HDG-FEM are 0.4% and 1.78%, respectively, which are significantly smaller than those of the reference solution. In contrast, the errors for the third-order CG-FEM with the same mesh size are 1.19% and 6.04%, indicating that the maximum value errors of the first-order HDG-FEM are smaller than those of the third-order CG-FEM. In terms of the L_∞ errors in Fig. 8b, it can be observed that for the same mesh size, the first-order HDG-FEM has lower L_∞ errors than the second-order CG-FEM, and the third-order HDG-FEM has lower L_∞ errors than the third-order CG-FEM. Regarding the L_2 errors in Fig. 8c, both HDG-FEM and CG-FEM exhibit similar error trends. However, the L_2 errors of the same-order HDG-FEM are lower than those of the same-order CG-FEM.

The varying requirements for the computational accuracy of the E-field in different regions of the head make the development of a hybrid order strategy in HDG-FEM a natural choice. Table 2 presents the variations of L_2 norm errors for different structures in the head using a hybrid order approach, with a total of 2.33 million tetrahedral elements and an average element size of 2.3 mm. In the 'Hybrid order' column, the sequence numbers from the first to the fourth digits represent the element orders for the skin, skull, CSF, and GM, respectively. The thin geometric structures of the skin, skull, and CSF allow for the use of the same element order within the same region without significantly increasing the computational burden, thereby eliminating the need for complex hybrid order strategies. Increasing the element order for a specific structure in Table 2 effectively reduces the L_2 error in that region. Considering the complex nested relationship between CSF and GM, a focused analysis is conducted. When the CSF order changed from first to third, the L_2 error decreased from 6.78 to 2.73% and further to 0.79%, indicating a significant improvement in accuracy. Furthermore, when a structure adopts higher-order elements, the L_2 error of the neighboring structure can be reduced to some extent. This is because DG-type methods are connected through numerical flux, and an improvement in the gradient accuracy in one region propagates through the numerical flux to other regions.

Computational time

Table 3 presents the number of global variables $\hat{u}$, the assembly time of the global matrix $\boldsymbol{K}$, and the time for solving $\boldsymbol{K}\hat{u} = b$ with different hybrid orders. The tetrahedral mesh used in Table 3 is identical to that used in Table 2. In terms of the number of global variables $\hat{u}$, transitioning from using first-order elements for the entire head to using second-order elements results in an increase factor of 1.99 (28.108/14.054). Similarly, transitioning from

Hybrid order	Number of û (million)	Assembly time of matrix K (s)	Time of solving K û = b (s)
1_1_1_1	14.054	563.18	210.56
1_1_2_1	19.595	998.21	352.15
1_1_3_1	26.982	1835.72	451.39
1_2_1_1	15.289	593.71	284.57
1_2_2_1	20.626	1191.21	369.90
2_1_1_1	14.924	575.18	263.94
2_1_2_1	20.464	1244.62	371.16
2_2_1_1	16.149	728.98	280.14
2_2_2_1	21.487	1102.09	381.88
2_2_2_2	28.108	1426.68	545.36
3_3_3_3	46.848	12188.02	1869.94

Table 3. The computational cost of HDG-FEM using hybrid order.

using first-order elements to using third-order elements results in an increase factor of 3.33 (46.848/14.054). The slow growth rate is attributed to the fact that in HDG-FEM, the solution variables for the global problem are only defined on the virtual surface of tetrahedral elements, whereas the interior nodes of the tetrahedra represent the solution variables for their respective local problems. From this perspective, the three-dimensional HDG-FEM can be considered as a special case of a 2D problem. In terms of global matrix assembly, the adoption of a hybrid order approach makes it challenging to utilize vectorized programming operations. In this study, the 'parfor' command in MATLAB is employed for assembly, which leads to a longer assembly time compared to the matrix solving time. There is still significant room for optimization in the assembly time of the global matrix. In terms of solving time, the iterative solver used in this study can reduce the relative residual of the problem with 2.33 million tetrahedra and third-order elements to 10^{-7} within 1869.94 s, which is equivalent to approximately half an hour.

Figure 9 clearly demonstrates the differences between HDG-FEM and CG-FEM in terms of the solution scale and solution time. In terms of DOF, CG-FEM at orders one to three have DOF values of 0.399 million, 3.148 million, and 10.583 million, with growth factors of 7.88 and 26.52, respectively. In contrast, HDG-FEM shows a comparatively slower increase in DOF, with growth factors of 1.99 and 3.33 as shown in Table 2. This indicates that CG-FEM has a higher rate of DOF increase with increasing element order than HDG-FEM. In terms of the solving time, comparing the black solid line and the red solid line in Fig. 9, for the first order, the total time of HDG-FEM is longer than that of CG-FEM. However, for the second and third orders, the total time of HDG-FEM is shorter than that of CG-FEM by 1074s (3045 − 1971) and 8427s (22484 − 14057) respectively. Considering that the CG-FEM results are obtained using the PDE module of COMSOL, where the assembly time of the global matrix is significantly shorter than the matrix solving time, it can be approximated that the total solution time in COMSOL represents the matrix solving time for CG-FEM. Comparing the black solid line and the blue solid line in Fig. 9, it can be observed that for the first to third order, the HDG-FEM matrix solving time is faster than CG-FEM by factors of 1.33 (281/210), 5.58 (3045/545), and 12.03 (22489/1869), respectively. The advantage is attributed to the fact that the HDG-FEM of the same order exhibits a sparser matrix structure compared to the CG-FEM of the same order[27,31,32] for the global matrix of HDG-FEM is a special two-dimensional problem matrix. And this demonstrates the significant potential of HDG-FEM in solving TMS problems.

Discussion

The computational time of HDG-FEM and CG-FEM in this study is provided as a reference, while ongoing research continues to make advancements in the global matrix assembly and matrix solving for both algorithms. Regarding the solver aspect, HDG-FEM and CG-FEM, as two different numerical methods, are expected to have different optimal solvers. However, in this study, the solution time of CG-FEM is represented by the solution time of the built-in solver in the mature commercial software, COMSOL, which still reflects the overall level of CG-FEM solvers currently available. In terms of matrix assembly of HDG-FEM, this study directly utilizes the "parfor" function in MATLAB to iterate over all elements. Further research is required to investigate more in-depth the assembly algorithms for global matrices when employing mixed-order elements.

The application of hybrid-order in HDG-FEM provides a new and flexible option for improving the accuracy of E-field calculations in TMS. Traditional numerical methods often employ local grid refinement or uniform usage of higher-order elements to improve the calculation accuracy of specific local details. In 3D cases, regardless of the method used, the rate of increase in DOF is faster than that when employing hybrid-order elements, resulting in a rapid increase in computational time. In summary, the application of hybrid-order elements makes the advantages of HDG-FEM over traditional numerical methods more pronounced.

The objective of this study is to demonstrate the potential of using hybrid-order HDG-FEM in the calculation of E-field in TMS problems with parameter mutation in thin layers, without considering all factors. For instance, the impact of brain structures such as the meninges and WM on the distribution of E-field in the head cannot be ignored, and the influence of anisotropic material parameters needs to be emphasized. Future research will fully consider the effects of various head structures and material anisotropy on the distribution of E-fields in the head and fully leverage the advantages of HDG-FEM.

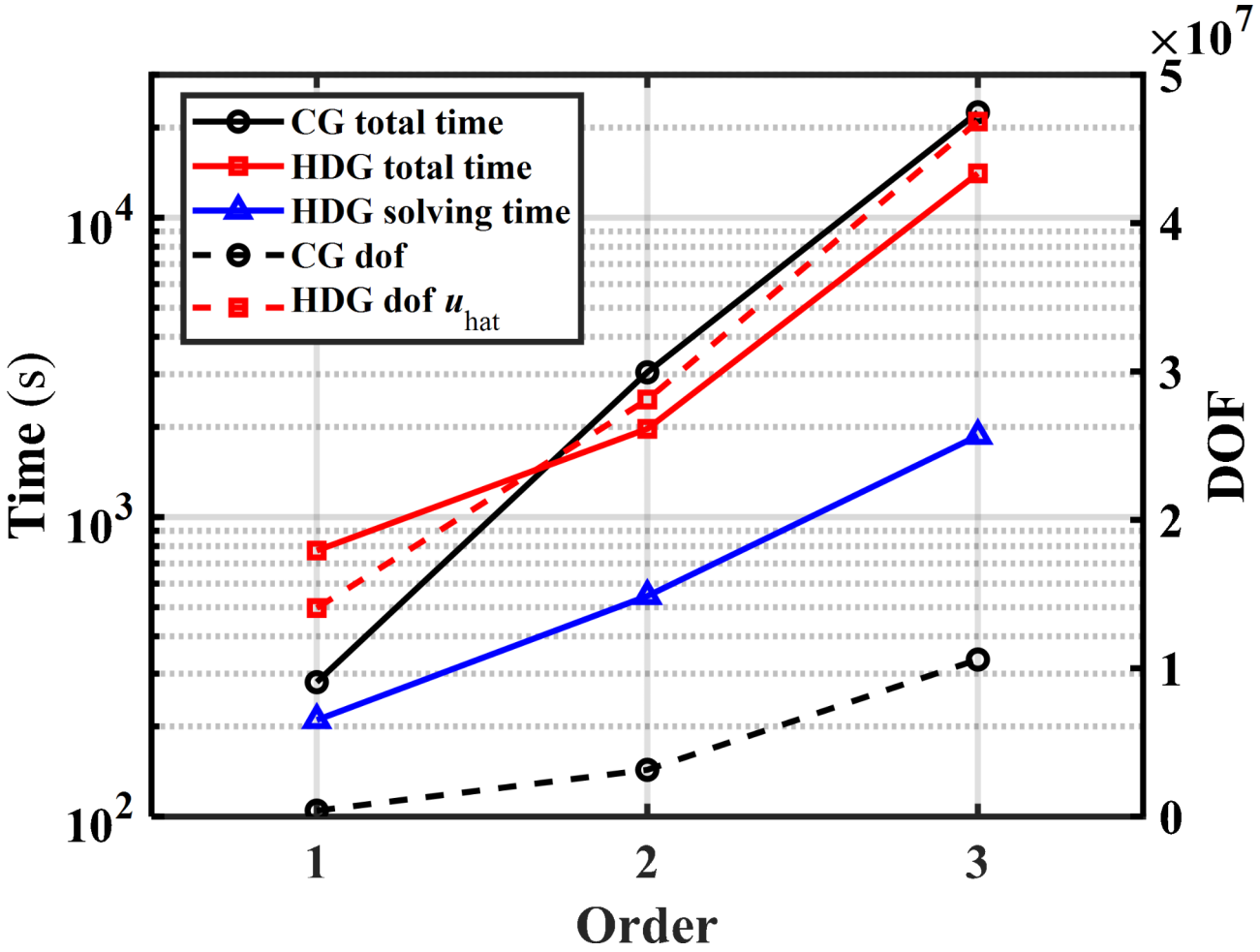

Fig. 9. Comparison of DOF and solving time for HDG-FEM and CG-FEM with a single element order on a 2.33 million tetrahedral mesh.

Conclusion

To address the issue of computing E-field in thin layers with electrical parameter mutation within the head structures, this study employs the HDG-FEM with hybrid order elements to solve TMS problems. First, starting from the discrete formulation of the HDG-FEM for the governing equations of TMS, this paper demonstrates the robust capability of HDG-FEM in computing E-field by referring to CG-FEM as a benchmark. Subsequently, the superior performance of HDG-FEM is elucidated through case studies on both modified and realistic head models, focusing on three aspects: computational error, computational cost, and the hybrid-order strategy. In terms of computational error, due to insufficient mesh refinement, the first-order CG-FEM may exhibit significant jumps in the E-field values, leading to noticeable deviations from the true solution. For the calculation of E-field in thin-layer regions with parameter mutation, the L_∞ norm error of the first-order HDG-FEM with the same tetrahedral mesh is comparable to the L_∞ norm error of the second-order CG-FEM. Moreover, the L_2 norm error of the same-order HDG-FEM is lower than that of the same-order CG-FEM. Regarding the computational cost, for the same number of mesh elements, HDG-FEM has significantly more global variables compared to CG-FEM. However, transitioning from first-order to third-order elements, the number of global variables in HDG-FEM increases by only 3.33 times, whereas in CG-FEM, it increases by 26.52 times. The solution speed of the global matrix for the third-order HDG-FEM is approximately 12.03 times faster than that of CG-FEM. In terms of the application of hybrid-order elements, employing higher-order elements in thin layers effectively reduces the maximum value error and L_∞ norm error of the E-field, whereas the L_2 norm error of the hybrid order HDG-FEM falls between those of the lowest and highest order. Finally, this study highlights the consistency between the characteristics of TMS E-field computation problems and the advantages of HDG-FEM, making it an alternative choice for addressing TMS computational issues.

Data availability

The authors declare that the data supporting the findings of this study are available within the paper and its supplementary information file.

Received: 29 June 2024; Accepted: 17 October 2024
Published online: 02 December 2024

References

1. Drakaki, M., Mathiesen, C., Siebner, H. R., Madsen, K. & Thielscher, A. Database of 25 validated coil models for electric field simulations for TMS. *Brain Stimul.* **15**(3), 697–706 (2022).
2. Johnson, M. D. et al. Neuromodulation for brain disorders: challenges and opportunities. *IEEE Trans. Biomed. Eng.* **60**(3), 610–624 (2013).
3. Lefaucheur, J.-P. In *Handbook of Clinical Neurology* (ed. Levin, K.H. & Chauvel, P.) 559–580 (Elsevier, 2019).
4. Barker, A. T., Jalinous, R. & Freeston, I. L. Non-invasive magnetic stimulation of human motor cortex. *Lancet* **325**, 1106–1107 (1985).
5. Nasseri, P., Nitsche, M. A. & Ekhtiari, H. A framework for categorizing electrode montages in transcranial direct current stimulation. *Front. Hum. Neurosci.* **9**, 54 (2015).
6. Thielscher, A., Antunes, A. & Saturnino, G. B. In 2015 37th Annual International Conference of the IEEE Engineering in Medicine and Biology Society (EMBC) 222–225 (2015).
7. Poljak, D. et al. On the use of conformal models and methods in dosimetry for nonuniform field exposure. *IEEE Trans. Electromagn. Compat.* **60**(2), 328–337 (2018).
8. Chang, S. et al. Twin coil design considerations for depth and focality in transcranial magnetic stimulation. *IEEE Trans. Magn.* **54**(11), 1–5 (2018).
9. Heller, L. & van Hulsteyn, D. B. Brain stimulation using electromagnetic sources: theoretical aspects. *Biophys. J.* **63**(1), 129–138 (1992).
10. Cvetković, M., Poljak, D. & Haueisen, J. Analysis of transcranial magnetic stimulation based on the surface integral equation formulation. *IEEE Trans. Biomed. Eng.* **62**(6), 1535–1545 (2015).
11. Saturnino, G. B., Puonti, O., Nielsen, J. D., Antonenko, D., Madsen, K. H., & Thielscher, A. In *Brain and Human Body Modeling: Computational Human Modeling at EMBC 2018* (eds Makarov, S., Horner, M. & Noetscher G.) (Springer, 2019).
12. Deng, Z.-D., Lisanby, S. H. & Peterchev, A. V. Coil design considerations for deep transcranial magnetic stimulation. *Clin. Neurophysiol.* **125**(6), 1202–1212 (2014).
13. Deng, Z.-D., Lisanby, S. H. & Peterchev, A. V. Electric field depth—focality tradeoff in transcranial magnetic stimulation: simulation comparison of 50 coil designs. *Brain Stimul.* **6**(1), 1–13 (2013).
14. Crowther, L. J., Porzig, K., Hadimani, R. L., Brauer, H. & Jiles, D. C. Realistically modeled transcranial magnetic stimulation coils for lorentz force and stress calculations during MRI. *IEEE Trans. Magn.* **49**(7), 3426–3429 (2013).
15. Carmona, I. C., Afuwape, O. F., Jiles, D. C. & Hadimani, R. L. Estimation of the focality of coils and quality of stimulation of biological tissues during transcranial magnetic stimulation. *IEEE Trans. Magn.* **58**(2), 1–6 (2022).
16. Shirinpour, S. et al. New tools for computational modeling of non-invasive brain stimulation in SimNIBS. *Brain Stimul. Basic Transl. Clin. Res. Neuromodul.* **14**(6), 1644 (2021).
17. Tang, B., Li, S. & Cui, X. A gradient weighted finite element method (GW-FEM) for static and quasi-static electromagnetic field computation. *Int. J. Comput. Methods* **17**(06), 1950017 (2020).
18. Wang, G., Guo, Z. B., Wang, Z. H. & Han, X. Transcranial stimulation analysis using the smoothed finite element method. *Comput. Methods Appl. Mech. Eng.* **391**, 114566 (2022).
19. Makarov, S. N. et al. A software toolkit for TMS electric-field modeling with boundary element fast multipole method: an efficient MATLAB implementation. *J. Neural Eng.* **17**(4), 046023 (2020).
20. Makarov, S. N., Noetscher, G. M., Raij, T. & Nummenmaa, A. A quasi-static boundary element approach with fast multipole acceleration for high-resolution bioelectromagnetic models. *IEEE Trans. Biomed. Eng.* **65**(12), 2675–2683 (2018).
21. Gomez, L. J., Dannhauer, M., Koponen, L. M. & Peterchev, A. V. Conditions for numerically accurate TMS electric field simulation. *Brain Stimul.* **13**(1), 157–166 (2020).
22. Weise, K., Wartman, W. A., Knösche, T. R., Nummenmaa, A. R. & Makarov, S. N. The effect of meninges on the electric fields in TES and TMS. Numerical modeling with adaptive mesh refinement. *Brain Stimul.* **15**(3), 654–663 (2022).
23. Hasgall, P. A., Di Gennaro, F., Baumgartner, C., Neufeld, E., Lloyd, B., Gosselin, M. C., Payne, D., Klingenböck, A., Kuster, N., IT'IS database for thermal and electromagnetic parameters of biological tissues, version 4.1, Feb 22, https://doi.org/10.13099/VIP21000-04-1. itis.swiss/database (2022)
24. Reed W. H., & Hill, T. R. *Triangular Mesh Methods for the Neutron Transport Equation*. Los Alamos Scientific Laboratory Report, LA-UR-73-479, **10**, 236 (1973).
25. Engwer, C., Vorwerk, J., Ludewig, J. & Wolters, C. H. A discontinuous Galerkin method to solve the EEG forward problem using the subtraction approach. *SIAM J. Sci. Comput.* **39**(1), B138–B164 (2017).
26. Hesthaven, J. S. & Warburton, T. *Nodal Discontinuous Galerkin Methods: Algorithms, Analysis, and Applications* 1st edn. (Springer, 2007).
27. Lee, E. G. et al. Investigational effect of brain-scalp distance on the efficacy of transcranial magnetic stimulation treatment in depression. *IEEE Trans. Magn.* **52**(7), 1–4 (2016).
28. Poljak, D. et al. On the use of conformal models and methods in dosimetry for nonuniform field exposure. *IEEE Trans. Electromagn. Compat.* **60**(2), 328–337 (2018).
29. Cockburn, B., Gopalakrishnan, J. & Lazarov, R. Unified hybridization of discontinuous Galerkin, mixed, and continuous Galerkin methods for second order elliptic problems. *SIAM J. Numer. Anal.* **47**(2), 1319–1365 (2009).
30. Ruben, S. & Huerta, A. Tutorial on hybridizable discontinuous Galerkin (HDG-FEM) for second-order elliptic problems. In *Advanced Finite Element Technologies* 105–129 (Springer International Publishing, 2016).
31. Giacomini, M., Sevilla, R. & Huerta, A. HDGlab: an open-source implementation of the hybridisable discontinuous Galerkin method in MATLAB. *Arch. Computat. Methods Eng.* **28**(3), 1941–1986 (2021).
32. Yamamoto, K., Takiyama, Y., Saitoh, Y. & Sekino, M. Numerical analyses of transcranial magnetic stimulation based on individual brain models by using a scalar-potential finite-difference method. *IEEE Trans. Magn.* **52**(7), 1–4 (2016).
33. Wang, W. & Eisenberg, S. R. A three-dimensional finite element method for computing magnetically induced currents in tissues. *IEEE Trans. Magn.* **30**(6), 5015–5023 (1994).
34. Chen, M. & Mogul, D. J. Using increased structural detail of the cortex to improve the accuracy of modeling the effects of transcranial magnetic stimulation on neocortical activation. *IEEE Trans. Biomed. Eng.* **57**(5), 1216–1226 (2010).
35. COMSOL: multiphysics software for optimizing designs. COMSOL. https://www.comsol.com/. Accessed Mar 23 2023.
36. The Population Head Model Repository, IT'IS Foundation website. https://www.itis.ethz.ch/virtual-population/regionalhuman-models/phm-repository/

Author contributions

LianyongWei wrote the main manuscript text and all authors reviewed the manuscript.

Funding
This work was supported by the National Natural Science Foundation of China under grant 52477009.

Declarations

Competing interests
The authors declare no competing interests.

Additional information
Supplementary Information The online version contains supplementary material available at https://doi.org/10.1038/s41598-024-76867-z.

Correspondence and requests for materials should be addressed to J.Z.